



HAL
open science

Characterization of the interface fracture energy dependency on mixed mode fracture between rigid fiber and soft matrix

P.-Y. Corbel, J. Jumel

► **To cite this version:**

P.-Y. Corbel, J. Jumel. Characterization of the interface fracture energy dependency on mixed mode fracture between rigid fiber and soft matrix. *Journal of the Mechanics and Physics of Solids*, 2024, 190, pp.105745. 10.1016/j.jmps.2024.105745 . hal-04812323

HAL Id: hal-04812323

<https://hal.science/hal-04812323v1>

Submitted on 30 Nov 2024

HAL is a multi-disciplinary open access archive for the deposit and dissemination of scientific research documents, whether they are published or not. The documents may come from teaching and research institutions in France or abroad, or from public or private research centers.

L'archive ouverte pluridisciplinaire **HAL**, est destinée au dépôt et à la diffusion de documents scientifiques de niveau recherche, publiés ou non, émanant des établissements d'enseignement et de recherche français ou étrangers, des laboratoires publics ou privés.



Distributed under a Creative Commons Attribution 4.0 International License



Characterization of the interface fracture energy dependency on mixed mode fracture between rigid fiber and soft matrix

P.-Y. Corbel^{*}, J. Jumel

ENSTA Bretagne, Institut de Recherche Dupuy de Lôme (UMR CNRS 6027), Brest, France

ARTICLE INFO

Keywords:

RCAIT
Rubber
Adhesion
Mixed mode fracture

ABSTRACT

An enhanced version of the Rubber Cord Adhesion Inflation Test (RCAIT) has been designed to experimentally assess the internal pressure and cable tension applied to the specimen needed to propagate a crack along the matrix/reinforcement interface. To calculate the critical strain energy release rate, we develop a semi-analytical model describing the deformation of a hyperelastic tube under loading conditions that reflect the ones applied experimentally. A more comprehensive numerical model of the test is also proposed to investigate the influence of loading conditions on rubber deformation near the crack tip. Comparison of different experimental data sets with the theoretical/numerical data demonstrates that the new experimental setup allows for a reliable determination of the rubber/cord interface failure envelope under combined loading conditions.

1. Introduction

Like other polymers, elastomers are mixed with particle fillers and reinforcements of diverse shapes, sizes, and types. This process aims to finely adjust and enhance their overall performance in terms of processability, durability, and thermal and mechanical properties. The inclusion of reinforcements allows for increased stiffness, strength, and toughness of materials, meeting the requirements of demanding applications including tires, anti-vibration components, piping, cables, medical prostheses, smart materials, and adhesives. The choice of particles, fibers, cables, or fabric materials must ensure compatibility with the polymer matrix to achieve the necessary adhesion between constituents. Indeed, this parameter significantly influences the failure modes and ultimate mechanical performances, particularly in terms of strength and toughness (Beter et al., 2020; Bonneric et al., 2019; Luo et al., 2023). Continuous efforts are being made to improve the reinforcement/polymer interface quality and the properties of the interphases formed within the polymer. This is achieved through surface treatment and conversion processes, in addition to new polymer chemistry compatible with more restrictive regulation (Crowther, 2001). However, adequate characterization tools, especially those related to mechanical properties, are crucial for assessing the adhesive performance of these interfaces and supporting ongoing developments.

This study aims to introduce a more versatile test protocol for characterizing the adhesion between fibrous reinforcement and an elastomer matrix, and more specifically the bonding between drawn steel wires and rubber, which are the components of tires. Currently, there are only a few tests available. Pull-out tests, as proposed by Gent et al. (1981), Nicholson et al. (1978) or described in standard procedures (Fielding-Russell et al., 1979), are generally used to assess adhesion between elementary filaments and the matrix (Meng and Chang, 2020). Additionally, peel or shear tests are conducted on reinforced rubber plies to complement the data (Rao et al.,

^{*} Corresponding author.

E-mail address: pierre.corbel@ensta-bretagne.org (P.-Y. Corbel).

Nomenclature

a	Sum of pre-crack and crack length, mm
a_0	Pre-crack length/initial unbonded region, mm
E	Strain energy, J
F_C	Critical axial force to crack propagation
F_{ext}	External axial force from tension load, N
F_z	Total axial force acting on the rubber envelop section, N
G	Strain energy release rate, kJ/m ²
G_C	Critical strain energy release rate, kJ/m ²
K	Modulus of the Exp-Ln strain potential, MPa
l	Specimen length, mm
p_1	Small strain parameter of the Exp-Ln strain potential, -
p_2	Large strain parameter of the Exp-Ln strain potential, -
P_C	Critical inflation pressure to crack propagation, bar
P_{ext}	External pressure/contact pressure of the rubber envelop, bar
P_{int}	Inflation pressure of the rubber envelop, bar
r	Radial coordinate in the deformed configuration, mm
r_{ext}	Deformed external radius of the rubber envelop, mm
r_{int}	Deformed internal radius of the rubber envelop, mm
R	Radial coordinate in the initial configuration, mm
R_{conf}	Radius of confinement tube, mm
R_{ext}	Initial external radius of the rubber envelop, mm
R_{int}	Initial internal radius of the rubber envelop, mm
s_i	Deviatoric stress tensor components, MPa
W	Hyperelastic strain energy density, J/mm ³
W_{tot}	Total external work, J
z	Axial coordinate in the deformed configuration, mm
Z	Axial coordinate in the initial configuration, mm
α	Crack tip angle, °
δa	Infinitesimal crack length increase, mm
ΔV	Injected volume variation, ml
λ_r	Radial elongation, -
λ_z	Axial elongation, -
λ_θ	Circumferential elongation, -
σ_i	Cauchy stress tensor components, MPa
σ_h	Hydrostatic stress, MPa

2004; Su et al., 2021). New experimental developments in this field are scarce. Nonetheless, a test inspired by the confined pressurized blister test (Dannenberg, 1961), named Rubber Cord Adhesion Inflation Test (RCAIT), has been developed recently with the sole purpose of evaluating the adhesion between a fibrous reinforcement and a polymer matrix, specifically an elastomer.

During the RCAIT, a pressurized fluid is injected into the interface between the matrix and the reinforcement to initiate and propagate a crack. The test specimen is obtained by embedding a single cord along the axis of a cylindrical rubber envelope. To prevent the rubber through-thickness failure and force the decohesion to propagate along the rubber/cord interface, the specimen is placed in a transparent rigid confinement tube that restricts the radial expansion of the rubber tube. Considerable effort has been made to refine the test protocol and analysis to consolidate the energy balance analysis used to calculate the critical Strain Energy Release Rate that governs the crack propagation condition.

The main limitation of most existing tests is the inability to precisely control the interface loading conditions. Indeed, the stress distribution is significantly affected by various experimental parameters such as specimen geometry, component mechanical properties, specimen loading conditions as well as experimental artifacts such as friction between the specimen and the fixture or between the cord and the matrix. Controlling and accurately predicting the mode mixity at the crack tip position is a challenging objective (Gent and Yeoh, 1982). It is worth noting that the loading conditions applied to the interface in real situations may differ significantly from those encountered during pull-out tests (Pupurs and Varna, 2017). This can be attributed to complex macroscopic loading, the effect of reinforced rubber layers' stacking sequence, or the interaction between the cords themselves (Bonneric et al., 2019). A modification of the RCAIT is proposed wherein internal pressure is applied simultaneously but independently on the reinforcement/matrix interface, along with tension load on the reinforcement. This modification allows for adjustment of the mode mixity at the crack tip position.

This article provides a detailed analysis of a novel experimental setup, along with the presentation of the results from a first series of tests carried out on rubber/brass plated cord assemblies. The main objective is to demonstrate the ability of the test to establish a failure envelope indicating the stable crack propagation onset conditions as a function of the values of the injected fluid pressure and

the tension applied to the cord. Following this, a mechanical model of the experiment is introduced to predict the deformation of the pre-crack specimen length considering combined axial loading, external (un)confinement, and internal pressure loading conditions. The energy balance analysis proposed for the classical RCAIT analysis is modified to account for the effect of axial tension and evaluate the strain energy release rate under these combined loading conditions. Moreover, supplementary finite element simulations are presented to clarify the relation between macroscopic and crack tip loading conditions.

2. Rubber/cord mixed mode adhesion test: RCAIT²

The RCAIT (see Fig. 1) was originally proposed as an alternative to the traditional H-test and Gent's test (Gent and Yeoh, 1982) for characterizing the adhesion between a rubber matrix and a single cord, filament, or strand reinforcement. The original test protocol is described in Kane et al. (2019), while subsequent improvements in the test fixture design and instrumentation are given in Corbel et al. (2022). The test specimen is obtained by curing a cylindrical rubber envelope around the cord in a mold so that the cord is located along the axis of the specimen. An anti-adhesive coating is applied to one side of the specimen to produce an artificial initial decohesion, the rest of the cord adheres to the rubber during the rubber vulcanization process due to the formation of strong Cu_xS covalent bonds (van Ooij, 1984, 1979).

A flange is also formed on the pre-crack side of the specimen during molding so that the specimen can be tightly connected to a hydraulic circuit from which a pressurized fluid is injected. The fluid flows inside the rubber envelope along the interface, inflating the precracked length. To prevent any crack propagation through the thickness of the rubber sheath due to an aneurysm, the specimen is placed in a confinement tube which limits the radial expansion of the specimen. A suitable lubricant (CRC® Silicon grease) is used to prevent any friction between the rubber and the tube which could limit the axial expansion of the specimen. The fluid is slowly injected until a critical pressure is reached, resulting in a stable self-similar propagation of the rubber-cord interface decohesion. Finally, by measuring the critical pressure, crack propagation, injected volume, and rubber deformation during the test, the critical strain energy release controlling the extent of the decohesion can be determined.

2.1. Experimental setup

The stress state at the crack tip, and consequently the mode mixity ratio, is not controlled in the classical RCAIT test set-up, as it depends on the geometry of the specimen. To allow the mode mixity to be tuned, a second loading condition is applied to the specimen. In the RCAIT, the pressurized fluid is slowly introduced by pressing a high-pressure stainless-steel syringe with a tensile testing machine. In the proposed Rubber Cord Adhesion Inflation Tension Test (RCAIT²) configuration, the specimen fixture is now placed in the tensile testing machine to pull off the cord under constant displacement rate conditions. Before the start of the pull-off load, the pressurized fluid is released into the pre-cracked part of the specimen from a hydro-pneumatic accumulator which maintains the pressure constant throughout the test.

A schematic view of the new setup is shown in Fig. 2. To obtain the necessary experimental data and to control the test conditions, various sensors and equipment are added to the system. A manual high-pressure pump (VIRAX® 262005 – 100 bar – 10 l) is used to fill the hydropneumatic accumulator, whose capacity is much greater than the volume injected into the specimen (11 vs ~ 15ml), thus ensuring a constant fluid pressure condition. A choke valve (Swagelok® SS-ORS2) is connected to the hydraulic circuit to release slowly the pressurized fluid. A pressure transducer (Swagelok® Model S Transducer – 250 bar) is also connected to the circuit to measure the fluid pressure during the test. Before the test, the hydraulic accumulator is filled with the appropriate pressure of nitrogen gas, which controls the minimum fluid pressure injected into the specimen. The tensile testing machine is equipped with a load cell to measure the tension applied to the cord. White dot markers are also deposited along the specimen and the specimen is observed during the test with a digital camera. The position of each marker is then determined using the markers tracking technique, then by analyzing the evolution of markers positions during the test, specimen elongation due to inner pressure and axial tension is determined so as the evolution of crack propagation during the test. A more detailed description of the metrological aspects of RCAIT is given in Corbel et al. (2022). The same methodology is applicable here when combined internal pressure and tension are applied to the specimen. In the following, a series of tests are performed to measure the evolution of the pull-out force during the stable crack propagation regime as a

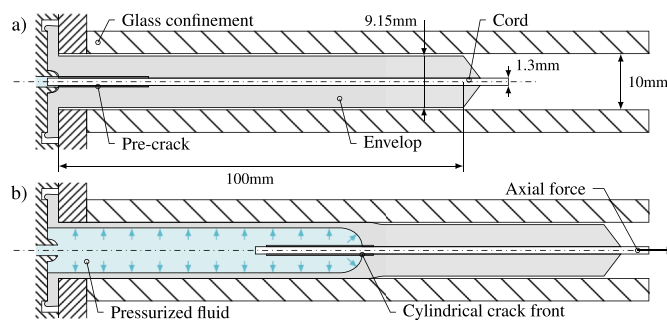


Fig. 1. Section of the Rubber Cord Adhesion Inflation Tension Test configuration in a) initial configuration, b) mixed inflation-tension pre-crack regime.

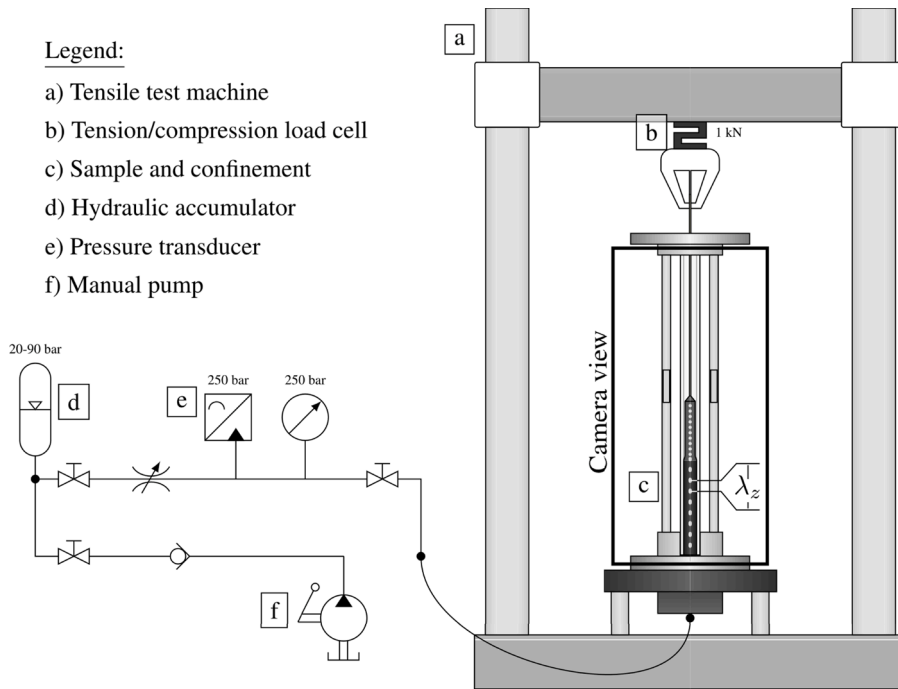


Fig. 2. Experimental setup with the hydraulic line, tensile machine, RCAIT, and sensors.

function of the injected fluid pressure. Then mechanical model of the sheave inflation is proposed to evaluate the value of the critical SERR which controls the crack propagation onset condition.

2.2. Results

A first series of tests are performed using the classical RCAIT protocol (no pull-out force, constant fluid injection rate). A typical fluid pressure vs injected fluid volume evolution is reported in Fig. 3. Nonlinear evolution is observed during prior stable crack propagation regimes due to rubber hyperelastic behavior also leading to geometrical nonlinearities. From the evolution of rubber envelope elongation, as a function of injected fluid pressure or using the evolution of injected fluid volume, the rubber mechanical behavior can be identified using a thick rubber tube inflation model. During the stable crack propagation regime, a stationary pressure evolution is observed. The mean pressure value is designated as the critical pressure, P_C , hereafter. The constant pressure is due to the steady-state nature of the crack propagation process. The measured critical pressure is equal to 83.1 bar with a standard deviation of 0.95 bar, the crack growth rate is controlled by the injection rate and equal here to 10 mm/min. When the process zone ahead of the decohesion reaches the end of the bonded length unstable crack propagation regime is observed as evidenced by the rapid pressure drop.

A second series of tests are then conducted but using the novel RCAIT² configuration to evaluate the effect of an additional pull-out

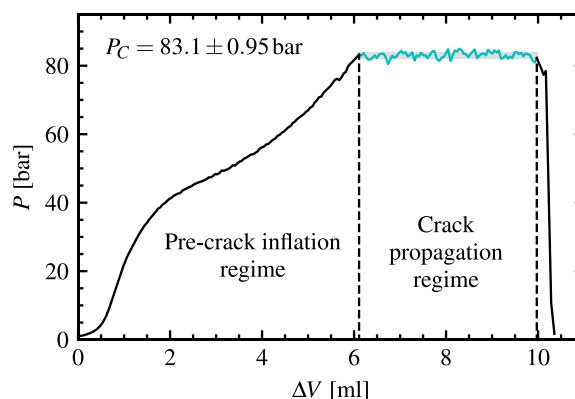


Fig. 3. Typical experimental evolution of pressure with injected volume for a pure pressure RCAIT (flow rate at 1 ml/min).

tension exerted on the cord. Fig. 4 reports the typical pressure and pull-out force evolutions with time recorded during a RCAIT². First, the pressurized fluid is slowly introduced from the accumulator (20 s < time < 40 s) into the specimen by opening the hydraulic circuit as detected by the progressive increase of the inflation pressure. Once a stable P_c value is reached, the pull-out test procedure is started. The pull-out force reaches a peak value which indicates the onset of the stable crack propagation regime. Then stationary pull-out force is recorded while the fluid pressure also remains constant (150 s < time < 270 s) until the decohesion reaches the specimen end and the final fracture is observed. The instant crack length evolution is also recorded from marker displacement analysis (Corbel et al., 2022), (see. Fig. 5.). The measured crack growth rate is 25 mm/min which corresponds to the crosshead displacement speed value.

Again, the stationary pull-out force and injected fluid pressure values recorded during the test suggest that the steady-state propagation hypothesis remains valid when a supplementary axial force is introduced. Therefore, the analytical method developed to analyze RCAIT results should be adapted to introduce the effect of the axial force.

3. Analytical model

The critical strain energy release rate is determined by performing a comprehensive energy balance of the crack propagation process, taking into account the work provided to drive the crack propagation, which is counterbalanced by various dissipative mechanisms. The framework applicable to RCAIT is primarily described in Kane et al. (2019). It takes advantage of the steady-state nature of the crack propagation process to establish a simple energy balance considering an infinitesimal extension of the crack length, δa (Pupurs and Varna, 2017). Now, by introducing an additional external force, the new energy balance is given by Eq. (1).

$$\delta W_{tot} = P_{int}\pi(r_{int}^2 - R_{int}^2)\lambda_z\delta a + F_{ext}(\lambda_z - 1)\delta a = 2\pi r_{int}G\delta a + \delta E \tag{1}$$

The term, $P_{int}\pi(r_{int}^2 - R_{int}^2)\lambda_z\delta a$, corresponds to the work done by the injection of the pressurized fluid, $F_{ext}(\lambda_z - 1)\delta a$, is the energy provided by the application of the tensile force to the cord. This energy is counterbalanced by the potential energy stored due to the deformation of the rubber, δE , and the effect of dissipative processes due to crack propagation, $2\pi r_{int}G\delta a$. It should be noted that G is an effective global quantity, since at a macroscopic scale no distinction can be made between the local dissipative damage mechanisms at the crack front scale and those at a more global scale related to the whole envelope deformation. For the time being, the main issue in the analysis of the test data is related to the evaluation of the potential energy stored in the rubber envelope, δE .

3.1. Constitutive equations

In the original version of the RCAIT, a Thick Tube Rubber Inflation Model (TTRIM) is derived and solved semi-analytically to simulate the expansion of the rubber envelope due to the application of internal pressure under unconfined and/or confined radial conditions. This model is now modified to introduce the application of an additional axial force.

The kinematic of thick tube inflation is identical when combining inflation- and axial tension loading conditions (Holzapfel et al., 2001). The TTRIM assumes incompressible rubber behavior and axisymmetric expansion of the cylindrical envelope in the cylindrical coordinate system, $(0, \vec{r}, \vec{\theta}, \vec{z})$. Assuming a constant elongation along \vec{z} , the elongations correspond to Eq. (2).

$$\lambda_r(r) = \frac{dr}{dR} \text{ and } \lambda_\theta(r) = \frac{r}{R} \text{ and } \lambda_z = \frac{z}{Z} \tag{2}$$

Thanks to these two main assumptions, the deformation of the specimen is completely determined in a large deformation framework by only two parameters (Skala, 1970):

$$\lambda_r^2(r) = \frac{1}{\lambda_z} \left[\frac{cr^2 - 1}{cr^2} \right] \tag{3}$$

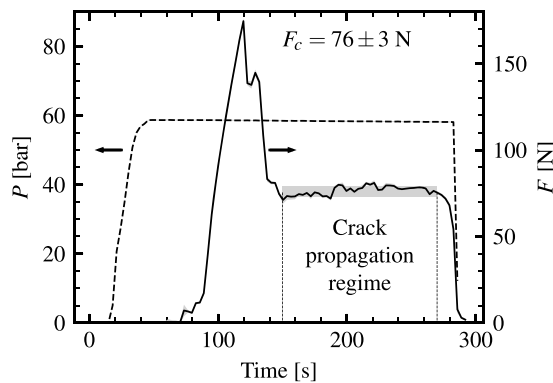


Fig. 4. Typical experimental evolution of inflation pressure and external force with time for a mixed inflation tension RCAIT². The inflation pressure is set at 60 bar with the pressure accumulator (displacement rate at 15 mm/min).

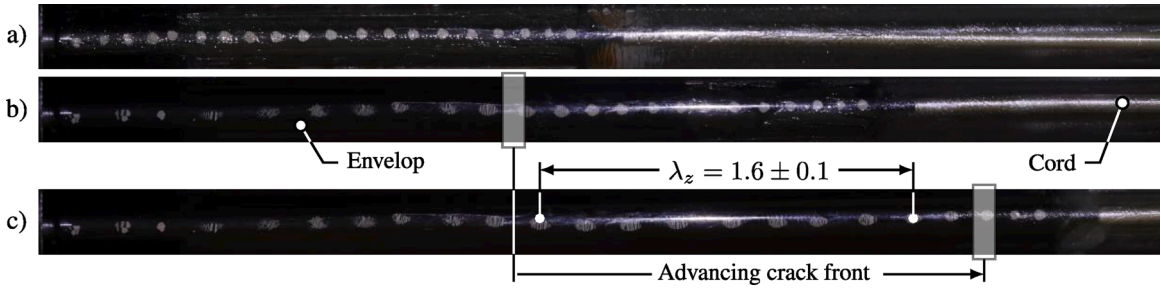


Fig. 5. Markers on the outer surface of the specimen a) undeformed configuration b) start of the force plateau c) end of the force plateau. Inflation pressure at 60 bar and displacement rate at 15 mm/min).

$$\lambda_{\theta}^2(r) = \frac{1}{\lambda_z} \left[\frac{cr^2}{cr^2 - 1} \right] \tag{4}$$

where, λ_z , $\lambda_{\theta}(r)$, and $\lambda_r(r)$ are the axial, circumferential, and radial expansion of the envelope respectively. c is an integration constant that will be determined from the boundary conditions for a given λ_z value. The radial position in the deformed state r is related to the radial position in initial state R with the Eq. (5).

$$r = \sqrt{\frac{1}{c} + \frac{R^2}{\lambda_z}} \tag{5}$$

With the specimen deformation being preliminarily defined by the incompressible axisymmetric expansion problem, the Cauchy stress distribution through the thickness can be determined for a given hyperelastic behavior of the rubber envelope. The mechanical behavior of the rubber is defined by a hyperelastic strain potential function, $W(\lambda_r, \lambda_{\theta}, \lambda_z)$, the parameters of which can be determined directly from RCAIT test data or alternatively from separate rubber characterization test methods. The Cauchy principal stress components, σ_i , are then given by the Eq. (6).

$$\sigma_i(r) = -\sigma_h(r) + \lambda_i \frac{\partial W}{\partial \lambda_i} = -\sigma_h(r) + s_i(r) \tag{6}$$

where σ_h is the hydrostatic pressure component and s_i are the principal deviatoric components. The expressions for s_i are obtained directly from the strain potential, W , using the expressions of the elongations given in Eqs. (3) and (4). In the following, an Exp-Ln hyperelastic behavior (Khajehsaeid et al., 2013) is considered whose strain energy function is given by Eq. (7).

$$W = K \left[\frac{1}{p_1} \exp(p_1(I_1 - 3)) + p_2(I_1 - 2)(1 - \ln(I_1 - 2)) - \frac{1}{p_1} - p_2 \right] \tag{7}$$

Material parameters K , p_1 and p_2 are identified using the method depicted in Corbel et al. (2022) and their values are respectively equal to 2.43 MPa, -1.91 and -0.545 .

The through thickness evolution of $\sigma_h(r)$ is found by solving the static equilibrium constitutive equation. Using the previous notation, this reduces to Eq. (8).

$$\frac{d\sigma_h}{dr} = \frac{ds_r}{dr} + \frac{s_r - s_{\theta}}{r} \tag{8}$$

With:

$$\sigma_h(r) = \sigma_h(r_{int}) + \delta\sigma_h(r) \tag{9}$$

Then considering Eq. (9) and integrating Eq. (8) we obtain:

$$\delta\sigma_h(r) = s_r(r) - s_r(r_{int}) + \int_{r_{int}}^{r_{ext}} \frac{s_r(u) - s_{\theta}(u)}{u} du \tag{10}$$

Again, it should be noted that the entire stress and strain distribution in the hyperelastic and incompressible tube is controlled by only two geometrical boundary conditions, such as r_{int} and r_{ext} . The stress distribution is determined up to an additive constant, $\sigma_h(r_{int})$, due to the incompressible nature of the rubber, which is determined with the boundary applied to the closed end of the tube.

$$2\pi \int_{r_{int}}^{r_{ext}} \sigma_z(u)u du = P_{int}\pi r_{int}^2 + F_{ext} \tag{11}$$

In Eq. (11), the left term corresponds to the contribution of the longitudinal stress component in the rubber sheath, the static equilibrium is obtained by applying the pressurized fluid on the closed end of the tube, so that the axial force exerted on the cord. After a few manipulations, the additive constant is obtained with Eq. (12).

$$\sigma_h(r_{int}) = \frac{2}{r_{ext}^2 - r_{int}^2} \left[\int_{r_{int}}^{r_{ext}} s_z u du - P_{int} r_{int}^2 - F_{ext} \right] \tag{12}$$

The geometry of the specimen and confinement tube inner radius are also important input parameters of the model. In the following, the outer radius of the specimen rubber envelope is equal to $R_{ext} = 4.575$ mm, the cord radius is equal to $R_{int} = 0.65$ mm and the inner radius of the confinement tube is equal to $R_{conf} = 5$ mm (see Fig. 1). Two different calculations should be performed to determine the strain and stress distribution in the elastomer envelope corresponding respectively to the confined and unconfined inflation regimes, due to the different boundary conditions encountered during the test. In the case of contact between the envelope and the confinement, the confined inflation solution (CIS) is obtained directly by using $r_{ext} = R_{tube}$ and using r_{int} as a control parameter to set the deformation of the rubber sheath. The axial force applied on the cord is then calculated as a function of the injected fluid pressure, considering $\sigma_r(r_{int}) = -P_{int}$ and using relations 8 and 11. In the unconfined inflation regime, the boundary condition, $\sigma_r(r_{ext}) = 0$, is again introduced, using r_{int} as control parameter. A Newton-Raphson procedure is then used to determine the r_{ext} value compatible with the loading condition (P_{int} , F_{ext}) applied to the specimen, as proposed in previous work (Kane et al., 2021), to find the unconfined inflation solution (UIS). A series of analytical simulations are then carried out using increasing applied axial force values for the constant pressure of the injected fluid, as would be done experimentally.

The results of the analytical simulation of the unconfined inflation regime are shown in Fig. 6. The evolutions of the inner and outer cylindrical envelope radius are represented as a function of the tension applied to the cord for various fluid pressures. Three different behaviors are observed. 1) For low fluid pressure, both the inner and outer radius decrease due to the Poisson effect, as the tube is essentially in pure tension. For high fluid pressure values, the inner and outer radius values increase simultaneously. The tube sustains biaxial stresses and the reduction of the net cross section facilitates the diametral expansion due to the inflation pressure. During the transition between these extreme situations, first the inner radius starts to increase with the tension applied to the cord, then the outer one. In the $56 \text{ bar} < P_{int} < 59 \text{ bar}$ range, the evolution of the outer radius with the tension applied to the cord is not monotonous. This behavior could be critical for the control of the test condition, since after the application of the initial pressure, an unconfined situation should be observed, but then, during the progressive application of the tensile load, the contact between the envelope and the confinement tube is established.

Fig. 7 also illustrates the intermittent nature of the contact between the rubber envelope and the confinement tube. The evolutions of the applied tensile force as a function of the inner rubber envelope radius are reported for various constant values of the injected fluid pressure. A grey shaded area is added to distinguish the situations where there is no contact or confined expansion. For Pressure values close to 55 bar, the contact may be intermittent since the $r_{int}(F_{ext})$ evolution is tangent to the shaded area.

We merge the UIS and CIS into the Mixed Inflation Solution (MIS) with the condition of contact $r_{ext} \geq R_{conf}$ in Fig. 8.

Using the confined or unconfined inflation/tension problem resolution to respect experimental condition, $r_{ext} < R_{conf}$, (mixed using inflation solution), the global energy balance analysis can be performed during the entire loading sequence to determine the Strain Energy Release Rate which controls the crack propagation condition.

3.2. SERR computation

The RCAIT² aims to evaluate the critical SERR that drives the decohesion process at the rubber/cords interface under mixed-mode loading conditions. To achieve this, the TTRIM model can be used to evaluate all the terms required in Eq. (1) and determine the

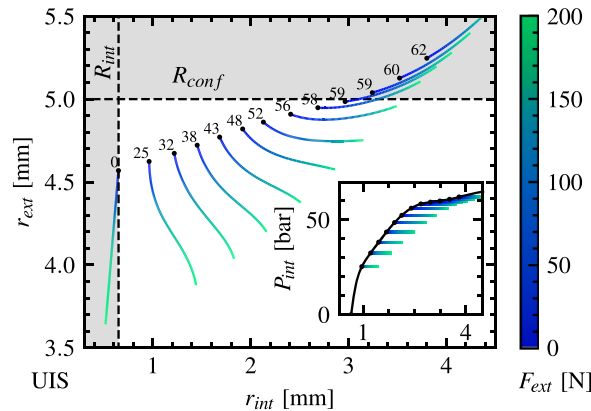


Fig. 6. Variation of the external and internal deformed radius with external force application at different inflation pressures in the unconfined boundary condition. Corresponding evolution of inflation pressure with the internal deformed radius reported in the insert.

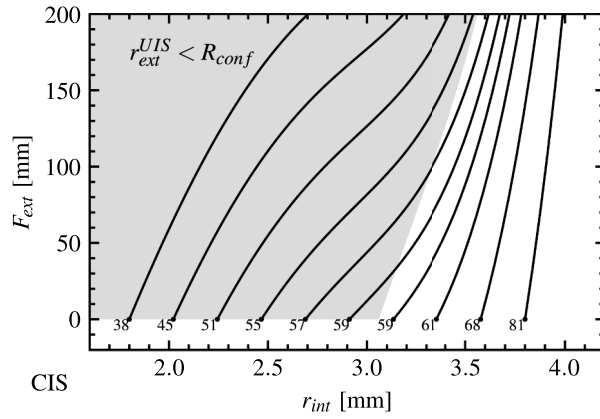


Fig. 7. Variation of the internal deformed radius with external force application at different inflation pressures in the confined boundary condition. Grey area corresponds to the contact clearance predicted with the UIS.

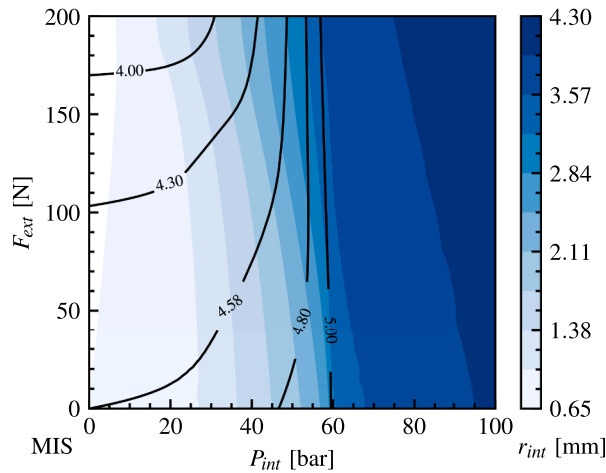


Fig. 8. Variation of the internal deformed radius with inflation pressure and externally applied force from the mixed inflation solution. Black lines correspond to isovalues of external deformed radius from the UIS.

intensity of the dual loading condition, (P_{int}, F_{ext}) , that causes the crack extension for a given critical SERR value, G_c . In Eq. (1), it is assumed that the overall behavior of the rubber envelope is hyperelastic and that dissipation is localized in the close vicinity of the rubber/cord interface. The potential energy stored in an infinitesimal length, δa , of the rubber envelope is then given by Eq. (13).

$$\delta E = 2\pi \int_{r_{int}}^{r_{ext}} W(r) r dr \delta a \tag{13}$$

$W(r)$ is obtained using the Eq. (7) and the values of λ_r and λ_z determined with the Eqs. (3) and (4). To complete the previous analysis, a series of analytical simulations were performed by varying F_{ext} in the interval [0–200]N and P_{int} in the interval [0–100]bar to map the specimen deformation and determine all relevant boundary conditions and output parameters, such as r_{int} , r_{ext} and λ_z . Then using Eq. (1), G is calculated. Fig. 9 represents with isovalue lines the evolution of the SERR as a function of applied load F_{ext} and P_{int} combined a colormap representing the evolution of longitudinal elongation. The relation between the SERR and the applied load is highly non-linear due to the nonlinear of the specimen deformation. The evolutions differ depending on whether crack propagation would occur with unconfined contact conditions (at the left side of the blue line “Contact”) or confined contact conditions (at the right side of the blue line). The SERR increases slowly with the pressure before contact, and accelerates after. The addition of axial force increases the SERR for a given pressure similarly before and after the contact. The loading condition leading to an inner tube radius smaller than the one of the cord which would lead to friction contact in practice is indicated with the dashed area. Such a condition is observed for low fluid inflation pressure value which varies with the applied pull-out force. Such friction contact is due to the Poisson effect in the rubber. The axial elongation increases slowly before the rubber/tube contact occurs and remains almost constant along an iso- G line. However, a strong variation of axial elongation is predicted after the rubber/tube contact condition occurs at constant G when increasing the axial load. Following the constant G line (e.g. 50 kJ/m²) from the pure pressure case to the pure tension case, the

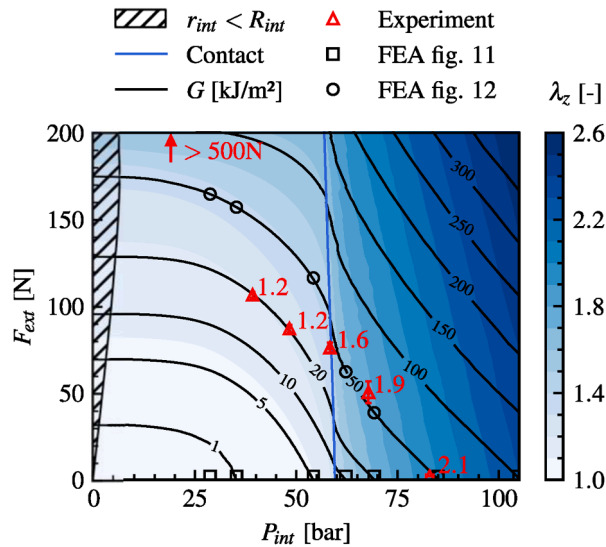


Fig. 9. Mapping of axial elongation and strain energy release rate depending on the inflation pressure and external force. The “Contact” line corresponds to the transition from unconfined to confined boundary condition. Dashed area corresponds to the theoretical internal friction region. Continuous lines are at equal strain energy release rate. The number in red beside the experimental point indicates the axial elongation during propagation. The error bar corresponds to the standard deviation of the measured pressure and force plateau.

axial elongation decreases with the increase of axial force. This counter-intuitive evolution is important to anticipate the specimen’s behavior during the test. Indeed, under combined loading conditions, the crack propagation rate is proportional to the crosshead displacement by a factor of $(1-\lambda_z)$. The final λ_z value during the crack propagation regime is important to control the crack propagation rate.

The pull-out forces measured for various injected fluid pressures are reported in Fig. 9 to evaluate the dependence of the critical SERR on loading conditions. The lowest fluid pressure used during this series of tests is equal to 20 bar but no plateau pull-out force evolution was observed during the crack propagation regime. For such a low inflation pressure value, an unconfined inflation regime is expected whatever applied pull-out force value together with a dramatic decrease of the specimen’s outer radius but also eventually of the inner radius. Such abnormal pull-out force evolution indicates that friction contact is susceptible to develop under such low injected fluid pressure conditions. For all tested conditions, cohesive failure is observed, and a residual rubber layer is observed on the surface of the cord for all tested conditions. Additionally, a larger residual rubber thickness is generally found at the initial crack tip position. Indeed, the crack initiation conditions differ from the crack propagation ones due to the presence of the PTFE insert used to obtain an artificial initial decohesion. In any case, the cord’s radius underestimates the effective rubber sheath inner radius. Therefore, the dashed area which indicates the loading conditions leading to friction contact between the rubber and the cord is certainly underestimated.

For all other test conditions plateau force evolution is observed together with a steady state crack propagation regime making SERR computation valid. The reference situation associated to only pressurized fluid injection indicates a 45.9 kJ/m² critical SERR value corresponding to 83.1 bar critical pressure value. When smaller fluid pressure is initially injected, an additional axial force is needed to propagate the crack. However, by reporting the resulting (P_c, F_{ext}) in Fig. 9 we observe that the combination of axial loading and inflation leads to reduce the critical energy release rate value from 50 kJ/m² to 20 kJ/m². A similar observation has been observed during peel tests by varying the peel angle (Liechti and Wu, 2001). The prediction of axial elongation at 1.2 in UIS is similar to the experiments. Fig. 9 reports the longitudinal elongations of the specimen measured with the marker monitoring technique. The observed elongations are close to the value predicted with the tube inflation model even if λ_z values are slightly overestimated. Again, this difference may be attributed to the underestimation of the rubber envelope’s inner radius.

This combined theoretical and experimental analysis leads to the main conclusion that the critical SERR controlling the rubber/cord decohesion process under mixed mode loading conditions tends to decrease with increasing the pull-off force intensity until friction contact between rubber and cord occurs. A finite element model is then proposed to investigate the influence of macroscopic loading conditions on the local strain/stress distribution in the vicinity of the crack tip.

4. Finite element analysis

The simulation of the complete test procedure is a complex task. As a preliminary analysis, a simple elastic finite element (FE) simulation with a still crack tip position at the interface between the cord and the rubber sheath is considered here. The same Exp-Ln hyperelastic model as the one introduced in Section 3 is used for the numerical simulation to describe the mechanical behavior of the rubber. The cord is modeled as a rigid body. It is assumed that the resulting stress/strain displacement is representative of the one that

would be observed during crack propagation despite the remaining rubber layer on the cord is not considered here. The boundary conditions and finite element mesh used as input for the Abaqus implicit solver are depicted in Fig. 10. Axisymmetric assumption is used reducing the model to a 2D one and thus reducing the computational time. The longitudinal displacement is blocked on the bottom part of the specimen (viz. $u_z(z = -50\text{mm}) = 0$). Kinematic coupling is introduced to bond the rubber to the cord whose displacement along the longitudinal axis is not constrained. The confinement tube is modeled as a fixed rigid body. A frictionless contact condition (node-to-surface with penalty enforcement) is assumed between the confinement tube and the rubber envelope. A uniform pressure is applied to the inner surface of the rubber tube and an axial pull-out force F_{ext} is applied to the rigid cord right edge. A spiderweb mesh structure centered around the crack tip position is used using triangular elements with quadratic interpolation (CAX6H) in the vicinity of the crack tip position. Quadrilateral elements (CAX8H) with lower density are used far from the crack tip position where a more uniform stress and strain distribution is observed.

Detailed analysis of the near crack tip region will not be developed here but the results from the FE simulations will be helpful to discuss the effect of loading condition (P_{int} , F_{ext}) on crack blunting. Fig. 11 represents the evolution of the rubber crack lip shape in the vicinity of the crack tip under pure pressure loading conditions for various SERR values as determined with the method given in Section 3. Two main effects should be outlined from this simulation. First, the crack tip angle between the rubber and the cord rapidly increases while the injection pressure increases. For high-pressure values, a blunted crack is obtained in the rubber rather than at the rubber/cord interface. Similar effects have also been observed for an interfacial crack between a rigid and a neo-hookean body (Krishnan and Hui, 2009) sustaining plane strain loading conditions. Under such a configuration a strong shear stress distribution develops along the interface despite the crack being macroscopically loaded under mode I condition due to the incompressible nature of the rubber and the contrast between the metallic cord and rubber stiffness.

In Fig. 12, the shapes of the rubber crack lip are shown for various combined loading conditions but leading to the same macroscopic $G = 50 \text{ kJ/m}^2$ value which corresponds to the one measured experimentally under pure internal pressure loading condition. The application of an additional pull-out force makes the crack tip opening sharper and reduces the crack tip blunting phenomenon for an equal SERR, the internal deformed radius decreases.

Generally, the addition of the addition of axial force increases the crack tip angle, with the variation depicted on Fig. 13. For a given SERR, i.e. 30 kJ/m^2 , the crack tip angle can vary from 16° to 140° with the increase of axial force and decrease of inflation pressure.

The experimental data presented in Fig. 9 are added in Fig. 13 by computing the crack tip angle corresponding to the axial force and inflation pressure during crack propagation. The experimental SERR appears to decrease with the increase of the angle. An angle of 16° results in an experimental SERR of around 50 kJ/m^2 , while at around 100° , the SERR decreases towards 20 kJ/m^2 . Note that the experiments giving a higher crack tip angle, i.e. purely pull-out load, have an internal friction problem. The internal radius tends to decrease with the addition of axial force (see Fig. 8) because of the thick-walled tube kinematic.

5. Discussion

The numerical results provide an insight into the load mixity influence on the crack tip hidden by the cylindrical rubber envelope. By balancing the inflation pressure and the axial force, multiple crack tip angles from 16° to 150° can be achieved. The experiments exhibit a strong load mixity dependence, with G_c ranging between 20 and 50 kJ/m^2 . Hence, reaching a specific crack tip angle appears difficult experimentally: α depends on both the proportion of pressure/force and the critical SERR. The RCAIT² can vary the crack mode mixity but cannot set it *a priori*. Furthermore, the geometry effect (i.e. smaller or larger R_{ext}) could modify the crack tip angle.

For a flat configuration, the equivalent test would be the Peel test (Bartlett et al., 2023) with a variable peel angle. The peel angle is related to the crack mode mixity and gives a metric of the SERR dependence on load type (shear or opening). The crack tip is visible on the peel configuration while hidden on the RCAIT, the only solution being conducting a test under a X-ray scan. Nonetheless, applying the peel test to a cord geometry or a ply of cord is tedious and the result will be heavily dependent on the geometry (distance between cords in the ply, number of cords, true fracture surface). Furthermore, the RCAIT has the advantage of keeping the crack propagating at the interface when the failure is cohesive (i.e. a residual layer of rubber on the cord) thanks to the axisymmetry on small radius geometry.

On the crack tip morphology, the finger-like shape in pure inflation is pulled forward by the addition of the axial force (Figs. 12 and 13). The variation of the crack tip angle could modify the crack surface position, transitioning from cohesive fracture for a low crack tip angle to adhesive fracture as it increases. The low crack angle keeps a singular stress (Krishnan and Hui, 2009) at the interface crack tip but locates a possible blunted crack away from the interface, which could explain the cohesive nature of the observed failure. However, without introducing a process zone with the correct physical length, a numerical model will not give the correct fracture morphology and behavior.

The fracture envelope in Fig. 13 could be compared to an equivalent on the peel test, with an analogy between the crack tip angle and the macroscopic peel angle. Therefore, the observed variation of the experimental G_c with α is the rubber cord adhesion agrees with the variation of SERR with peel angle reported in the literature on the rubber peel test (Cook et al., 1997). Establishing a common mode mixity metric between the peel test and the RCAIT² should however require much more experimental and numerical work, perhaps with a local approach.

6. Conclusion

A novel experimental setup is proposed to evaluate the critical SERR controlling the decohesion between a metal cord and a rubber sheath sustained mixed mode loading conditions. The novel test configuration consists is a combination of the RCAIT and pull-out tests.

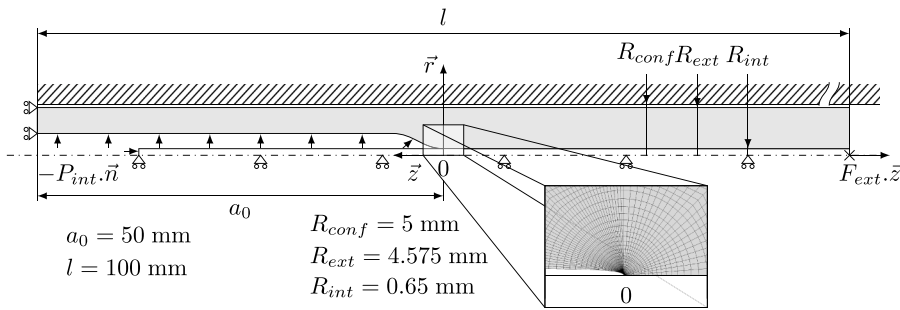


Fig. 10. Finite element model of crack front analysis with geometry, boundary conditions and mesh.

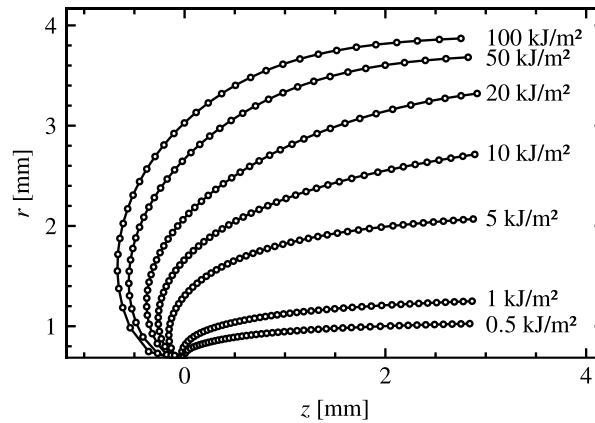


Fig. 11. Comparison of crack tip opening profiles for an increasing strain energy release rate under pure pressure load.

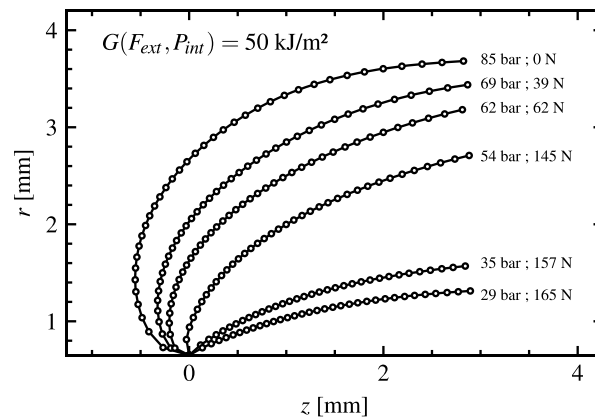


Fig. 12. Comparison of crack tip opening profiles for a constant strain energy release rate with different pressure-tension load mixity.

A semi-analytical model is derived to evaluate the specimen SERR under combined pull-out force and internal pressure loading conditions and take into confined or unconfined rubber envelope conditions during the crack propagation. A failure envelope characterizing the combined pull-out force and internal pressure values leading to stable crack propagation is obtained from a series of tests which exhibits a noticeable decrease of the critical SERR when the pull-out force contribution increases. However, for small internal pressure values, friction contact between the rubber and the cord is suspected leading to a large increase of the critical SERR which is not predicted with the actual model. Preliminary finite element analyses are performed to evaluate the influence of the combined loading condition on the shape of the crack tip which evidences that the crack tip angle decreases significantly with increasing injected pressure so that no stress singularity is observed anymore but blunted crack tip configuration. Due to the application of pull-out force, the crack tip angle is increasing, and sharp crack tips are observed again which mostly explains the decrease of critical SERR under combined loading conditions.

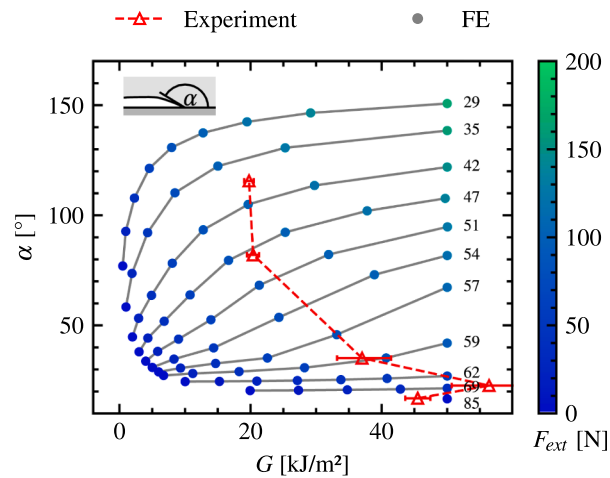


Fig. 13. Variation of the crack tip angle from the finite element model with the strain energy release rate for multiple iso- P_{mt} (corresponding pressure in bar) with an increasing axial force. The experimental critical strain energy release rate points are added with the corresponding crack tip angle computed numerically.

The proposed RCAIT² is an original technique to evaluate the decohesion processes between a fiber reinforcement and a matrix. The rubber/cords configuration reveals complex effects leading to a complex failure envelope. Supplementary theoretical and experimental activities should now be engaged to achieve a better understanding of the damage and dissipative mechanisms in the vicinity of the crack tip which are involved in the failure process.

CRedit authorship contribution statement

P.-Y. Corbel: Conceptualization, Data curation, Formal analysis, Investigation, Methodology, Software, Visualization, Writing – original draft, Writing – review & editing. **J. Jumel:** Conceptualization, Funding acquisition, Project administration, Resources, Supervision, Validation, Writing – review & editing.

Declaration of competing interest

The authors declare the following financial interests/personal relationships which may be considered as potential competing interests:

P.-Y. Corbel reports equipment, drugs, or supplies was provided by Michelin Technology Center in Ladoux. If there are other authors, they declare that they have no known competing financial interests or personal relationships that could have appeared to influence the work reported in this paper.

Data availability

Supplementary material document includes the experimental data.

Acknowledgements

The authors wish to acknowledge M. Daude of MFP Michelin for the supply of RCAIT specimens and Dr. T. Rey of MFP Michelin for industrial support. P.-Y. Corbel acknowledges the ENSTA Bretagne and the Region Bretagne (ARED grant) for the PhD funding.

Supplementary materials

Supplementary material associated with this article can be found, in the online version, at [doi:10.1016/j.jmps.2024.105745](https://doi.org/10.1016/j.jmps.2024.105745).

References

Bartlett, M., Case, S.W., Kinloch, A., Dillard, D., 2023. Peel tests for quantifying adhesion and toughness: a review. *Prog. Mater. Sci.* 137, 101086 <https://doi.org/10.1016/j.pmatsci.2023.101086>.

- Beter, J., Schrittester, B., Meier, G., Fuchs, P.F., Pinter, G., 2020. Influence of fiber orientation and adhesion properties on tailored fiber-reinforced elastomers. *Appl. Compos. Mater.* 27, 149–164. <https://doi.org/10.1007/s10443-020-09802-w>.
- Bonneric, M., Aubin, V., Durville, D., 2019. Finite element simulation of a steel cable - rubber composite under bending loading: influence of rubber penetration on the stress distribution in wires. *Int. J. Solids Struct.* 160, 158–167. <https://doi.org/10.1016/j.ijsolstr.2018.10.023>.
- Cook, J.W., Edge, S., Packham, D.E., 1997. The adhesion of natural rubber to steel and the use of the peel test to study its nature. *Int. J. Adhes. Adhes.* 17, 333–337. [https://doi.org/10.1016/S0143-7496\(97\)00024-9](https://doi.org/10.1016/S0143-7496(97)00024-9).
- Corbel, P.-Y., Jumel, J., Kane, K., Mbiakop-Ngassa, A., 2022. Refined crack propagation methodology and energy balance analysis in the Rubber Cord Adhesion Inflation Test. *Int. J. Adhes. Adhes.* 119, 103243 <https://doi.org/10.1016/j.ijadhadh.2022.103243>.
- Crowther, B.G., 2001. *Handbook of Rubber Bonding*. iSmithers Rapra Publishing.
- Dannenberg, H., 1961. Measurement of adhesion by a blister method. *J. Appl. Polym. Sci.* 5, 125–134. <https://doi.org/10.1002/app.1961.070051401>.
- Fielding-Russell, G.S., Nicholson, D.W., Livingston, D.I., 1979. Physical factors in cord-to-rubber adhesion by a new tire cord adhesion test. *Tire Reinf. Tire Perform.* <https://doi.org/10.1520/STP36950S>.
- Gent, A.N., Fielding-Russell, G.S., Livingston, D.I., Nicholson, D.W., 1981. Failure of cord-rubber composites by pull-out or transverse fracture. *J. Mater. Sci.* 16, 949–956. <https://doi.org/10.1007/BF00542739>.
- Gent, A.N., Yeoh, O.H., 1982. Failure loads for model adhesive joints subjected to tension, compression or torsion. *J. Mater. Sci.* 17, 1713–1722. <https://doi.org/10.1007/BF00540799>.
- Holzapfel, G.A., Gasser, T.C., Ogden, R.W., 2001. A new Constitutive Framework for Arterial Wall Mechanics and a Comparative Study of Material Models. In: Cowin, S.C., Humphrey, J.D. (Eds.), *Cardiovascular Soft Tissue Mechanics*. Springer Netherlands, Dordrecht, pp. 1–48.
- Kane, K., Jumel, J., Lallet, F., Mbiakop-Ngassa, A., Vacherand, J.-M., Shanahan, M.E.R., 2019. A novel inflation adhesion test for elastomeric matrix /steel cord. *Int. J. Solids Struct.* 160, 40–50. <https://doi.org/10.1016/j.ijsolstr.2018.10.012>.
- Kane, K., Jumel, J., Mbiakop-Ngassa, A., Lallet, F., Vacherand, J.-M., Shanahan, M.E.R., 2021. Rubber cord adhesion inflation test: effect of constitutive rubber model on evaluation of G. *Eng. Fract. Mech.* 244, 107547 <https://doi.org/10.1016/j.engfracmech.2021.107547>.
- Khajehsaeid, H., Arghavani, J., Naghdabadi, R., 2013. A hyperelastic constitutive model for rubber-like materials. *Eur. J. Mech. A Solids* 38, 144–151. <https://doi.org/10.1016/j.euromechsol.2012.09.010>.
- Krishnan, V.R., Hui, C.-Y., 2009. Finite strain stress fields near the tip of an interface crack between a soft incompressible elastic material and a rigid substrate. *Eur. Phys. J. E* 29, 61–72. <https://doi.org/10.1140/epje/i2009-10452-4>.
- Liechti, K.M., Wu, J.-D., 2001. Mixed-mode, time-dependent rubber/metal debonding. *J. Mech. Phys. Solids* 49, 1039–1072. [https://doi.org/10.1016/S0022-5096\(00\)00065-X](https://doi.org/10.1016/S0022-5096(00)00065-X).
- Luo, G., Guo, J., Zhang, C., Yang, X., 2023. Life prediction of cord/rubber laminates under multiaxial fatigue. *Int. J. Fatigue* 174, 107733. <https://doi.org/10.1016/j.ijfatigue.2023.107733>.
- Meng, Q., Chang, M., 2020. Interfacial crack propagation between a rigid fiber and a hyperelastic elastomer: experiments and modeling. *Int. J. Solids Struct.* 188–189, 141–154. <https://doi.org/10.1016/j.ijsolstr.2019.10.006>.
- Nicholson, D.W., Livingston, D.I., Fielding-Russell, G.S., 1978. A new tire cord adhesion test. *Tire Sci. Technol.* 6, 114–124. <https://doi.org/10.2346/1.2150999>.
- Pupurs, A., Varna, J., 2017. Steady-state energy release rate for fiber/matrix interface debond growth in unidirectional composites. *Int. J. Damage Mech.* 26, 560–587. <https://doi.org/10.1177/1056789515624000>.
- Rao, S., Daniel, I.M., Gdoutos, E.E., 2004. Mechanical properties and failure behavior of cord/rubber composites. *Appl. Compos. Mater.* 11, 353–375. <https://doi.org/10.1023/B:ACMA.0000045312.61921.1f>.
- Skala, D.P., 1970. Modified equations of rubber elasticity applied to the inflation mechanics of a thick-walled rubber cylinder. *Rubber Chem. Technol.* 43, 745–757. <https://doi.org/10.5254/1.3547285>.
- Su, B., Liu, S., Zhang, P., Wu, J., Wang, Y., 2021. Mechanical properties and failure mechanism of overlap structure for cord-rubber composite. *Compos. Struct.* 274, 114350 <https://doi.org/10.1016/j.compstruct.2021.114350>.
- van Ooij, W.J., 1984. Mechanism and theories of rubber adhesion to steel tire cords—an overview. *Rubber Chem. Technol.* 57, 421–456. <https://doi.org/10.5254/1.3536016>.
- van Ooij, W.J., 1979. Fundamental aspects of rubber adhesion to brass-plated steel tire cords. *Rubber Chem. Technol.* 52, 605–675. <https://doi.org/10.5254/1.3535231>.